



Article

A Modified Method for Reducing the Scale Effect in Land Surface Temperature Downscaling at 10 m Resolution

Zhida Guo ^{1,2}, Lei Cheng ^{1,2,*}, Liwei Chang ^{1,2}, Shiqiong Li ^{1,2} and Yuzhu Li ^{1,2}

¹ State Key Laboratory of Water Resources Engineering and Management, Wuhan University, Wuhan 430072, China; gzd1225@whu.edu.cn (Z.G.); liweichang@whu.edu.cn (L.C.); lishiqiong@whu.edu.cn (S.L.); liyuzhu@whu.edu.cn (Y.L.)

² Department of Hydrology and Water Resources, School of Water Resources and Hydropower Engineering, Wuhan University, Wuhan 430072, China

* Correspondence: lei.cheng@whu.edu.cn

Abstract: Satellite-derived Land Surface Temperature (LST) plays an important role in research on natural energy balance and water cycle. Considering the tradeoff between spatial and temporal resolutions, accurate fine-resolution LST must be obtained through the use of LST downscaling (DLST) technology. Various methods have been proposed for DLST at fine resolutions (e.g., 10 m) and small scales. However, the scale effect of these methods, which is inherent to DLST processes at different extents, has rarely been addressed, thus limiting their application. In this study, a modified daily 10 m resolution DLST method based on Google Earth Engine, called mDTSG, is proposed in order to reduce the scale effect at fine spatial resolutions. The proposed method introduces a convolution-based moving window into the DLST process for the fusion of different remote sensing data. The performance of the modified method is compared with the original method in six regions characterized by various extents and landscape heterogeneity. The results show that the scale effect is significant in the DLST process at fine resolutions across extents ranging from 100 km² to 22,500 km². Compared with the original method, mDTSG can effectively reduce the LST value differences between tile edges, especially when considering large extents (>22,500 km²) with an average R^2 improvement of 33.75%. The average MAE is 1.63 °C, and the average RMSE is 2.3 °C in the mDTSG results, when compared with independent remote sensing products across the six regions. A comparison with in situ observations also shows promising results, with an MAE of 2.03 °C and an RMSE of 2.63 °C. These findings highlight the robustness and scalability of the mDTSG method, making it a valuable tool for fine-resolution LST applications in diverse and extensive landscapes.

Keywords: LST downscaling; scale effect; remote sensing; fine resolution



Citation: Guo, Z.; Cheng, L.; Chang, L.; Li, S.; Li, Y. A Modified Method for Reducing the Scale Effect in Land Surface Temperature Downscaling at 10 m Resolution. *Remote Sens.* **2024**, *16*, 3908. <https://doi.org/10.3390/rs16203908>

Academic Editor: Dimitris Kaskaoutis

Received: 29 August 2024

Revised: 9 October 2024

Accepted: 17 October 2024

Published: 21 October 2024



Copyright: © 2024 by the authors. Licensee MDPI, Basel, Switzerland. This article is an open access article distributed under the terms and conditions of the Creative Commons Attribution (CC BY) license (<https://creativecommons.org/licenses/by/4.0/>).

1. Introduction

Land Surface Temperature (LST) is an important parameter for determining various biological and physical processes [1–4]. LST time-series derived from satellite data provide valuable information and enable the comprehensive monitoring of dynamic changes in LST at different resolutions [5–7]. These data have been widely applied in various fields, including urban heat island effect estimation [8–10], crop production prediction [11–13], fire monitoring [14–16], and soil moisture assessment [17–19]. The current operational satellites are unable to provide LSTs with both fine temporal and spatial resolutions, due to tradeoffs caused by the balance between cost and technology [20]. The demand for fine spatial (<30 m) and temporal (<daily) resolutions in numerous applications has become increasingly urgent [21–23]. To effectively address this challenge, many LST downscaling (DLST) techniques have been proposed, which enhance the spatiotemporal resolution of satellite-derived LSTs through the fusion of multiple data sources [5,24–27]. However, many previous studies have demonstrated that the scale effect widely exists in the DLST

process, especially when complex heterogeneous surface features/materials are contained within the pixel at fine resolutions [28–30].

Previous studies have developed many downscaling techniques. Wang et al. [31] proposed the Adaptive Area-to-Point Regression Kriging (ATPRK) algorithm to overcome the non-stationarity of spatial features. Jin et al. [32] combined geographically weighted regression and ATPRK to solve the problems of spatial heterogeneity and spatial correlation and successfully downscaled the spatial resolution from 25 km to 1 km. Liu et al. [33] used STARFM to obtain LST products with fine resolution. While these studies have demonstrated remarkable results, the premise assumption used in the downscaling process was that the LST–descriptor relationship (linear or non-linear) at the original (coarse) resolution remains scale-invariant at finer resolutions [34]. This often leads to discrepancies between the DLST and the true LST at fine resolutions [35], which is known as the scale effect.

This view has been confirmed by many researchers who have pointed out that the LST–descriptor relationship is variable in landscapes with different surface feature heterogeneities [36–39]. For example, Chen et al. [36] investigated the impact of scale effects on the modeled relationship between the vegetation index (VI) and LSTs in grassland and observed that the established VI–LST coefficients at the original resolution (900 m) were almost three times as high as those at the fine resolution (90 m). Zhou et al. [37] evaluated the scale effect using five different linear regression models and found that the scale effect was closely related to spatial variations in the LST and the scale factor at both the coarse and target resolutions. In addition, many studies have demonstrated that the scale effect is particularly sensitive to changes in the spatial resolution and spatial extent [28–30,40]. Jeganathan et al. [28] showed that the scale effect varies significantly at different resolutions, and a root-mean-square error (RMSE) below 2 °C can only be achieved within the range of 270 m to 990 m. Pu and Bonafoni [29] comparatively analyzed the DLST results at different resolutions from 6 m to 62 m and found that the scale effect was particularly pronounced at finer resolutions (<30 m); this remained evident even after correction. Pu [30] analyzed the DLST results at different resolutions and spatial extents using semivariograms and observed that the results were unreliable if the spatial resolution and spatial extent lag distance were less than the range (20–30 m) measured via semivariograms. These studies have confirmed that the scale effect tends to be more pronounced at fine resolutions. However, most studies have focused on resolving the scale effect at moderate resolutions, and very few researchers have attempted to resolve scale effects at fine resolutions.

Various attempts have been made to minimize the impact of the scale effect at moderate resolutions [29,41–44]. For example, Bindhu et al. [41] showed that the used descriptors present spatial scale effects depending on the satellite sensor’s resolution, allowing for calibration of the LST–descriptor relationship during the downscaling process. Pu and Bonafoni [29] proposed a new method with a correction term (CT), which directly corrects the scale effect through considering the heterogeneity degree of surface features within a pixel region at a specific resolution. Although these methods have achieved a certain degree of success, their handling is cumbersome, and they are computationally inefficient. The use of a moving window, as another factor affecting the scale effect in the DLST process, has received widespread attention due to its ease of operation and significant benefits. Garrigues et al. [42] found that, when the moving window was set to less than 100 m, the spatial variability in vegetation cover at the landscape scale could be well captured, thus greatly reducing the scale effect of the non-linear estimation process of land surface variables. Zakšek and Oštir [43] successfully reduced the influence of the scale effect using the relationship between the principal components and LST to establish a regression equation within the moving window. Gao et al. [44] evaluated the global window and local window strategies and finally formulated an indirect criterion based on aggregation–disaggregation in order to reduce the scale effect effectively. The use of a moving window allows for good performance to be achieved at moderate resolutions; however, few studies have used such an approach to address the scale effect in fine-resolution downscaling processes.

The method proposed by Mhawej and Abunnasr [45]—namely, Daily Ten-ST-GEE (DTSG)—successfully implements 10 m daily DLST images using MODIS and Sentinel-2 data. In this study, DTSG is used as a baseline method to evaluate the scale effect at fine resolutions. It has the following two main advantages: first, it is a fully automated, user-friendly, easily accessible, and open-source DLST system that can significantly reduce research costs; second, it is deployed on Google Earth Engine (GEE) cloud platform, improving the efficiency and portability of computation. Based on this, a modified DTSG (mDTSG) method is proposed, which aims to achieve fine-resolution DLST outputs in any spatial extent through the introduction of a convolution-based moving window. Multiple data sources are used to validate the performance and reliability of mDTSG. The main objectives of this study are as follows: (1) To evaluate the scale effect in DLST results with fine resolutions (10 m) under different spatial extents and heterogeneous landscapes; (2) to evaluate and validate the accuracy and usability of the proposed mDTSG method; and (3) to explore the performance of mDTSG in terms of reducing the influence of scale effects when considering different extents and heterogeneous landscapes.

The rest of the paper is structured as follows: Section 2 presents the data, methods, and case study area. Section 3 presents the downscaling evaluation results of the original model and the modified model. Section 4 discusses the influencing factors of the moving window and the uncertainty of the results. Section 5 concludes the paper.

2. Materials and Methods

2.1. Proposed Method of mDTSG

2.1.1. Process of LST Downscaling

The DLST process in the mDTSG method is divided into four steps: namely, (1) data pre-processing, (2) system error correction, (3) regression relationship establishment, and (4) LST downscaling. The method is summarized in the flowchart shown in Figure 1.

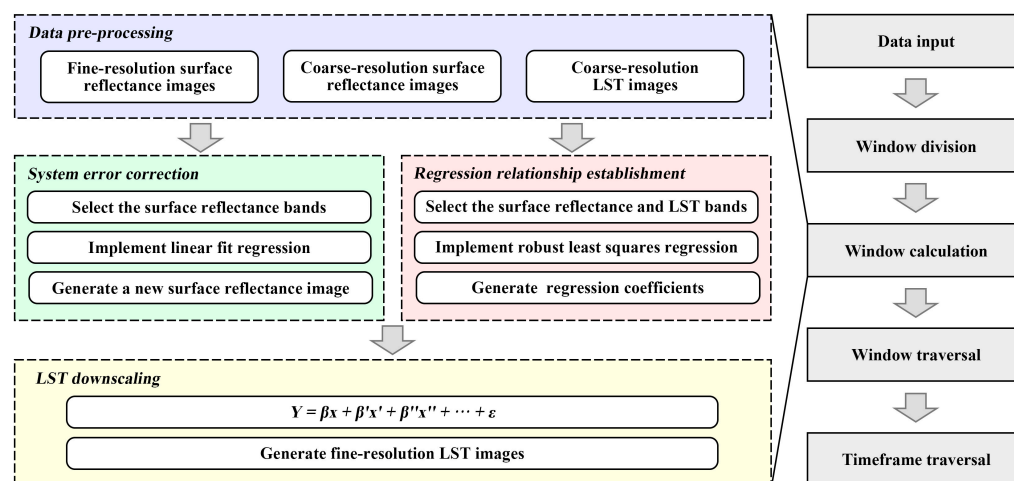


Figure 1. The flowchart of the mDTSG algorithm. The implementation steps of mDTSG are shown on the right, and the DLST implementation steps in the “window calculation” are shown on the left.

In the first step, the model pre-processes the input coarse-resolution LST and fine- and coarse-resolution surface reflectance remote sensing data sets. The pre-processing process is detailed in Section 2.3. The pre-processed data all have a daily temporal resolution.

Considering the differences in sensor acquisition time, instantaneous field of view, orbiting geometry, swath width, and spectral response functions, which can result in image discrepancies, system error correction is performed. We assume that, for a given area, images acquired on the same date between different satellite sensors are comparable and correlated after radiometric calibration, geometric correction, and atmospheric correction. We utilized this correlation to eliminate system error caused by different sensors. Linear fit regression is conducted between the spatially fine- and coarse-resolution surface reflectance

remote sensing data, as suggested by Claverie et al. [46] and Zhang et al. [47]. The fine-resolution image is used as the independent variable, and the coarse-resolution image is used as the dependent variable with bandpass adjustments for the blue (B), green (G), red (R), near-infrared (NIR), shortwave infrared 1 (SWIR-1), and shortwave infrared 2 (SWIR-2) bands. Then, the fine-resolution values are corrected to coarse-resolution values and applied to the entire image, with the exception of no-data values. Following this process, a new six-band fine-resolution surface reflectance image is created, which effectively eliminates the system error between the two different satellite sensors.

Then, the regression relationship between surface reflectance and LST is established. The corresponding weight coefficients for each band are obtained using statistical robust least squares (RLS) regression analysis, with coarse-resolution surface reflectance images and five-fold upscaled coarse-resolution LST images as the independent variables and coarse-resolution LST images as dependent variables. It is worth noting that coarse-resolution LST images that are five-fold upscaled are included as independent variables, with the aim to first smoothen the values at the edges of each tile utilizing coarse-resolution information entropy reduction. The second reason for this is to correct the regression results, to a certain extent, such that the simulated results and remote sensing observations are within a reasonable error range. For the choice of the regression method, we refer the reader to the study of Abunnasr and Mhawej [48] for details, which indicates that RLS has the best effect.

The DLST results are calculated using the following equation:

$$Y = \beta x + \beta' x' + \beta'' x'' + \dots + \varepsilon, \quad (1)$$

where x , x' , and x'' are the independent variables, including the six bands of the new fine-resolution surface reflectance image and the LST band of the coarse-resolution LST image; β , β' , and β'' are the weighting coefficients of each band after RLS regression analysis; and ε is the residuals of the modeled relationship.

2.1.2. Implementation of the mDTSG Method

The complete workflow of the mDTSG model, which is executed entirely on GEE, consists of five parts: (1) Data input, (2) window division, (3) window calculation, (4) window traversal, and (5) timeframe traversal (Figure 1).

The model uses three types of data as inputs: Coarse-resolution LST and fine- and coarse-resolution surface reflectance remote sensing data. The selected study area is then divided based on the size of the moving window. Figure 2 shows the schematic diagram of the moving window operation. The moving window is designed in the form of spatial convolutions. There are two adjustable parameters: namely, the receptive field range (i.e., a square of size $a \times a$) and the convolution kernel range (square of size $b \times b$). Differing from traditional spatial convolution, the convolution kernel range is not limited to the minimum pixel level, and the receptive field range does not need to be a multiple of the convolution kernel range. Both can use a flexible spatial range, allowing the selection of a range that contains any pixels. The selected study area is divided into windows of size $b \times b$. For each window, the data within the $a \times a$ range centered on it is taken as input, while the computed output only retains the $b \times b$ range. The two parameters can be adjusted independently to achieve the best DLST effect. For this study, after thorough testing, the range of the convolution kernel for the moving window was selected as $0.1^\circ \times 0.1^\circ$ and the range of the receptive field was selected as $0.01^\circ \times 0.01^\circ$ (we refer the reader to Section 4.1 for further details). It is worth noting that the window at the edge of the study area is calculated with some outward expansion of the exceeding part, such that the data source can fill the entire window and give full play to the available data.

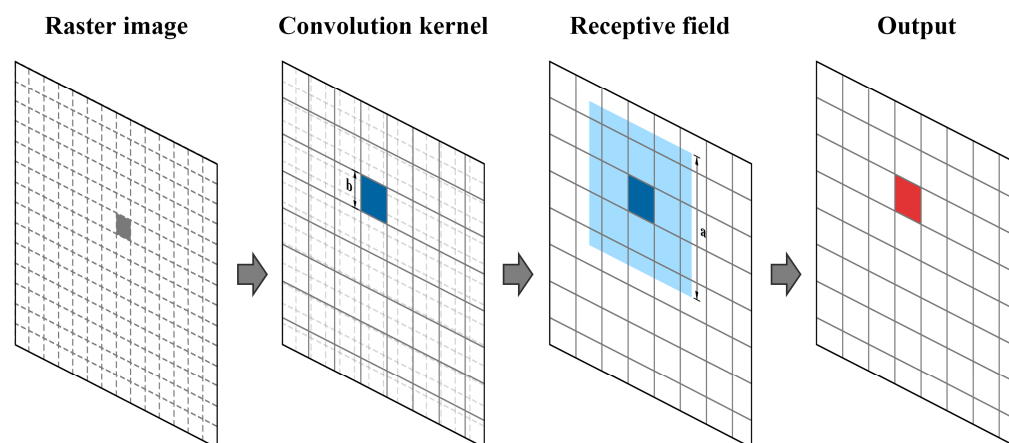


Figure 2. Schematic diagram of the moving window. The gray square is a pixel of the raster image. The dark blue square represents the convolution kernel range. The light blue square represents the receptive field range. The red square represents the output range.

In the window calculation, the process described in Section 2.1.1 is performed within each available window (here, the available window refers to a moving window with sufficient pixels). If the percentage of no-data pixels in a window is greater than or equal to 95%, the number of image pixels in the window is considered insufficient to support the computation, and the window is automatically skipped. The DLST images in all windows are then pieced together to generate a fine-resolution LST image within the study area. When all of the above steps are completed, the algorithm is transferred to the next day until all computations are completed within the given timeframe.

2.2. Case Study Area

Six sites (shown in Figure 3(a1–a6)) within China with different land cover types (including forest, shrubs, grass, urban, crops, and water) were selected as the case study areas, in order to fully assess the applicability of the model. The forest region (31.71°N, 109.35°E) is located at the junction of Chongqing, Hubei, and Shanxi Provinces and is characterized by a sub-tropical monsoon climate. The shrubs region (43.91°N, 116.43°E) is located in the Inner Mongolian Plateau, which experiences a typical temperate continental climate. The grass region (34.87°N, 101.62°E) is located on the south side of the Qilian Mountains, which has a plateau alpine climate and sparse vegetation. The urban region (39.91°N, 116.39°E) is located in Beijing, one of the largest urban agglomerations in China. The crops region (47.83°N, 125.87°E) is located in the Northeast China Plain, which has a typical temperate monsoon climate. The water region (29.18°N, 116.24°E) is located in Poyang Lake which, as the largest freshwater lake in China, has obvious seasonal characteristics. The six regions have significant differences and unique characteristics, making them relevant representatives for assessing the DLST results.

Temperature data from a meteorological station were selected for validation. Danjiangkou station (32.56°N, 111.50°E) is located in the Danjiangkou Reservoir, Hubei Province, as shown in Figure 3(b1,b2). It belongs to the sub-tropical monsoon climate zone, with an average annual precipitation of 804 mm and an average annual temperature of 15.7 °C. The coldest month is January, with a mean temperature of 2.3 °C and an extreme minimum temperature of −16.5 °C. The hottest month is July, with a mean monthly temperature of 27.5 °C and an extreme maximum temperature of 41 °C. The number of days annually with a stable mean daily temperature exceeding 5 °C is 282. The drastic temperature variations result in significant differences in LST, which is helpful for validation and analysis of the DLST results.

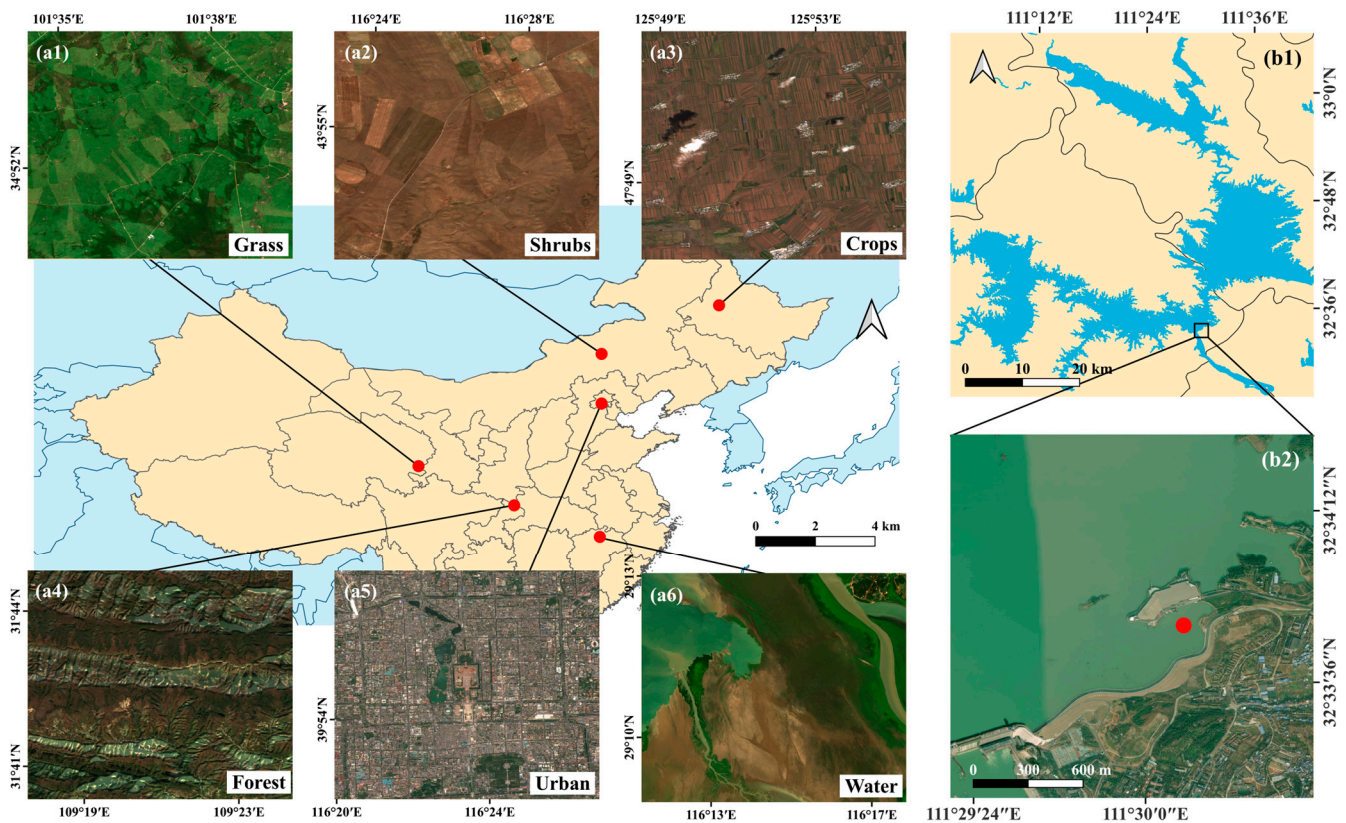


Figure 3. Location of the case study areas. The six different surface cover types correspond to: (a1) Grass; (a2) shrubs; (a3) crops; (a4) forest; (a5) urban; and (a6) water. (b1) Overall map of the Danjiangkou Reservoir; and (b2) specific location of the Danjiangkou station, which is the red dot in the figure.

2.3. Data

2.3.1. Remote Sensing Data

Sentinel-2 and MOD09A1 products were used as the fine- and coarse-resolution surface reflectance inputs, respectively, and the MOD11A1 product was used as the coarse-resolution LST input for mDTSG in this study. All three data sets are available directly from the GEE platform. The Sentinel-2 satellite, launched on 23 June 2015 under the Global Monitoring for Environment and Security (GMES) program, a joint initiative of the European Commission and the European Space Agency, carries a multispectral imager (MSI) that captures data in 13 spectral bands with 10 m spatial resolution and a 5-day revisit period (Sentinel-2 MSI: MultiSpectral Instrument, Level-2A). MODIS, which is a large-scale satellite-based remote sensing instrument developed by NASA, provides the MOD09A1 and MOD11A1 data sets. MOD09A1 offers surface reflectance in 7 bands with 500 m resolution and an 8-day revisit period [49], while MOD11A1 provides LST and emissivity values with 1000 m resolution and a daily revisit period [50]. MOD09A1 and MOD11A1 have been accessible since February 2000, while the Sentinel-2 data set has only been available since January 2018. Considering that the mDTSG system uses images from all three products simultaneously, for the period before 2018, Sentinel-2 data sets can be replaced by the Sentinel-2 MSI: MultiSpectral Instrument, Level-1C products, which require further atmospheric correction.

The Landsat-8 data set was used to evaluate the DLST results. This product, which is also available on GEE, is provided by the U.S. Geological Survey (USGS). It is generated from the Thermal Infrared Sensor (TIRS) onboard the Landsat-8 satellite, providing data in 2 thermal infrared bands with 100 m resolution and a 16-day revisit period. The Landsat-8 image acquisition time is 10:00 a.m. locally. The data set is processed by the Rochester

Institute of Technology (RIT) and NASA Jet Propulsion Laboratory (JPL) using a single-channel algorithm involving parameter and atmospheric corrections [51]. It is worth noting that the LST band (ST_B10) has been resampled to 30 m in the USGS Landsat 8 Level 2 product, in order to match the Operational Land Imager (OLI) band.

Sentinel-2, Landsat-8, and MOD09A1 all contain cloudy pixels, which need to be eliminated through a simple cloud masking process before use. Landsat-8 and MOD09A1 use the cloud masking function provided by GEE, while the Sentinel-2 data set contains the “CLOUDY_PIXEL_PERCENTAGE” attribute, which can be used to filter images directly. For this study, only images with less than 20% cloud coverage were selected. As the data provided by GEE exhibit some stretching bias, calibration needs to be carried out to obtain the actual values. LST data uniformly use Celsius degrees.

As each data set was obtained from different sensors with different processing, they need to be unified before further calculations can be performed. First, for the coordinate system and resolution of images, WGS84 was used as the standard to reproject all images. MOD09A1 was resampled with a spatial resolution of 1000 m to match MOD11A1 for regression analysis. The resampling method used the average aggregation algorithm that was provided by GEE. To match the daily temporal resolution of MOD11A1, Sentinel-2 and MOD09A1 were selected 8 days before and after the target date for median assessment. Daily data sets were obtained after processing. Second, for the image bands, the surface reflectance data in this study require six bands: B, G, R, NIR, SWIR-1, and SWIR-2. It was necessary to filter and rename the bands of all surface reflectance data sets such that they could be retrieved uniformly for subsequent calculations. MOD11A1 only requires the “LST_Day_1km” band, while Landsat-8 only needs the “ST_B10” band.

2.3.2. In Situ Water Surface Temperature Observation

The in situ data from the Danjiangkou station were used to validate the DLST results. Danjiangkou station was completed and put into operation in early 2022. It is equipped with a 20 m water body temperature chain (CS225), which can observe the water body temperature with an accuracy of ± 0.2 °C at a 10-layer gradient and calculate the water body temperature profile. Data are acquired and stored by a CR1000X data collector every 30 min. The CS225 and CR1000X are from Campbell Scientific United Kingdom in China. Only the land surface water temperature was used in this study.

Considering that the validation process requires the use of both remote sensing and in situ data, time alignment of each datum was performed in this study. The validation time range selected was from 8 April 2022, to 2 November 2022, with 36 days available after screening. The daily transit time of the Terra satellite equipped with MODIS is 10:30 a.m. locally; thus, in situ data captured at the same time were selected.

The data used in the study are detailed in Table 1. For ease of description, all results produced by DTSG or mDTSG are collectively referred to as simulated values in the following, and all values used for evaluation and validation are collectively referred to as observed values.

Table 1. Summary of the data sets used in this study.

Name	Usage	Spatial Resolution	Temporal Resolution
Sentinel-2	Surface reflectance	10 m	5 day
MOD09A1	Surface reflectance	500 m	8 day
MOD11A1	LST	1000 m	1 day
Landsat-8	LST	30 m	16 day
Danjiangkou station data	LST	-	30 min

2.4. Method Performance Evaluation and Validation

To evaluate the scale effect of the fine-resolution DLSTs, a study was conducted at six study areas with different surface cover types based on DTSG. Squares measuring 10 km × 10 km, 60 km × 60 km, and 150 km × 150 km were set as the study extents. The regions for comparison were set as 10 km × 10 km, consistent with the minimum extent of the study area.

The mDTSG was evaluated using the best practices described by Guillevic et al. [52]; in particular, the 10 m results of mDTSG were three-fold upscaled to 30 m and compared to the 30 m Landsat-8 product. The implementation was divided into two steps. First, spatial co-registration was performed for both MOD11A1 and Landsat-8 products. The processed LST showed a systematic error due to the difference in acquisition time and observation wavelength between MOD11A1 and Landsat-8 products. As the mDTSG results were derived from the MOD11A1 product, which has system error with respect to Landsat-8 products; the normalization method proposed by Pu and Bonafoni [29] was used in this study to effectively address this issue. The Landsat-8 product was upscaled to 1000 m resolution, in order to match MOD11A1. Then, 1000 m Landsat-8 was subtracted from MOD11A1 to obtain the pixel-based LST difference (dT). The dT was resampled back to 30 m and then added to the initial 30 m Landsat-8 to achieve spatial co-registration between MOD11A1 and Landsat-8. Second, the 30 m mDTSG and co-registered 30 m Landsat-8 were compared.

In total, 50,000 points were randomly selected for comparisons at the six study sites with an extent of 150 km × 150 km. After removing null points and anomalies, 41,214 points in forest, 49,725 points in shrubs, 37,791 points in grass, 49,266 points in urban, 47,597 points in crops, and 16,967 points in water were left. Least squares regression analysis was performed on all points, in order to obtain the evaluation results. Considering different seasonal influences, different times were randomly selected for comparison in different regions, ensuring image availability. The randomly selected dates for the six regions were 12 November 2020 for forests; 25 September 2019 for shrubs; 18 August 2020 for grass; 29 May 2019 for urban; 22 September 2019 for crops; and 24 March 2021 for water.

The validation of mDTSG required utilization of the observed LST data from Danjiangkou station. As in the evaluation process, there are also system errors between in situ and remote sensing data due to differences in observation wavelengths and data processing. Linear fit regression of the 36 MOD11A1 and in situ data pairs was carried out to solve this problem. The calculated coefficients were then applied to the in situ data, in order to obtain a measured LST time-series based on MOD11A1 correction. Finally, the mDTSG and measured LST results were compared. Validation results were obtained by performing least squares regression analysis on 36 pairs of data. To further explore the accuracy of the simulated LST of mDTSG, we also analyzed the distribution trend between the simulated LST and the LST observed at Danjiangkou station in the time-series. Considering that the Danjiangkou station is surrounded by water and the LST was almost the same at the same time point, it was considered reasonable to use the temperature of one 1000 m × 1000 m pixel of MOD11A1 to represent the LST at the station.

The coefficient of determination (R^2), mean absolute error (MAE), and root-mean-square error (RMSE) were selected as assessment indices. R^2 reflects the ability of the model to explain the data, and MAE and RMSE reflect the absolute difference between the simulated value and the observed value. The calculation formulas for the R^2 , MAE, and RMSE are as follows:

$$R^2 = 1 - \frac{\sum_{i=1}^m (T_{obs(i)} - T_{sim(i)})^2}{\sum_{i=1}^m (T_{obs(i)} - \overline{T_{obs(i)}})^2} \quad (2)$$

$$MAE = \frac{1}{m} \sum_{i=1}^m |T_{sim(i)} - T_{obs(i)}|, \quad (3)$$

$$RMSE = \sqrt{\frac{1}{m} \sum_{i=1}^m (T_{sim(i)} - T_{obs(i)})^2}, \quad (4)$$

where T_{sim} is the mDTSG model's simulated value from MOD11A1, T_{obs} is the observed value from Landsat-8 or the in situ measurements used for evaluation and validation, and m is the number of samples.

3. Results

3.1. Scale Effect of LST Downscaling

Figure 4 shows the results of the original DLST method for different study areas and different extents. For different extents, it can be clearly observed that the spatial scale effect becomes increasingly obvious as the extent increases. When applying DTSG to $10 \text{ km} \times 10 \text{ km}$ (Figure 4(a1–f1)), the features in each study area could be obviously detected, and the DLST performance is significant. With the expansion to $150 \text{ km} \times 150 \text{ km}$ (Figure 4(a3–f3)), the image details were gradually lost. Among them, the scale effect for shrubs, grass, and water regions is more sensitive to the change in the extent. When expanding to $60 \text{ km} \times 60 \text{ km}$, the details of these three regions (Figure 4(b2,c2,f2)) were almost lost, exhibiting obvious grid boundaries and approaching the MOD11A1 data source. Expanding to $150 \text{ km} \times 150 \text{ km}$, the image quality (Figure 4(b3,c3,f3)) remained almost unchanged. In contrast, the scale effect for the forest, urban, and crops regions increased more slowly. Expanding to $60 \text{ km} \times 60 \text{ km}$, the LST of the forest region (Figure 4(a2)) became homogenized, and the overall temperature difference became smaller. The urban and crops regions (Figure 4(d2, e2)) changed little, and only the number of high-temperature pixels increased. Expanding to $150 \text{ km} \times 150 \text{ km}$, the forest and crops regions (Figure 4(a3,e3)) presented distinct grid boundaries, while the urban region (Figure 4(d3)) still maintained distinctive feature characteristics and did not change much. For the different study areas, overall, the scale effect has the least impact in the urban region and the most impact in the water region. At $10 \text{ km} \times 10 \text{ km}$, the water region (Figure 4(f1)) already presented a distinct grid boundary, while the other regions showed good performance.

3.2. Evaluation and Validation of Proposed Method

Figure 5 shows the results of the evaluation carried out in the six study areas. It can be observed that the points in the six regions are concentrated near the 1:1 line, and the overall average R^2 is 0.56. Compared with the original method, R^2 increases by 33.75% on average (Table 2, see Figure A1 for more details). The average MAE is 1.63°C , and the average RMSE is 2.3°C , which is slightly different from the original method and is within a reasonable error range. The forest and urban regions presented significantly higher values, possibly affected by the different acquisition times of the two satellite sensors resulting in a shift in the shadow location (north of the forest region and northwest of the urban region in Figure A2) offset, which can produce large errors. The shrubs and crops region values (Figure 5b,e) were lower and well simulated due to their flat terrain, simple features, and lack of disturbance factors within the two regions. It can also be observed that the slopes in all regression expressions were less than 1, indicating that the simulated LST overestimates the low-temperature regions and underestimates the high-temperature regions, leading to an overall homogenization trend. However, the degree of deviation is not high and falls within a reasonable error range. The results show that mDTSG can perform well in different research areas, which proves its universality (to a certain extent), such that it can provide strong support for research in various fields.

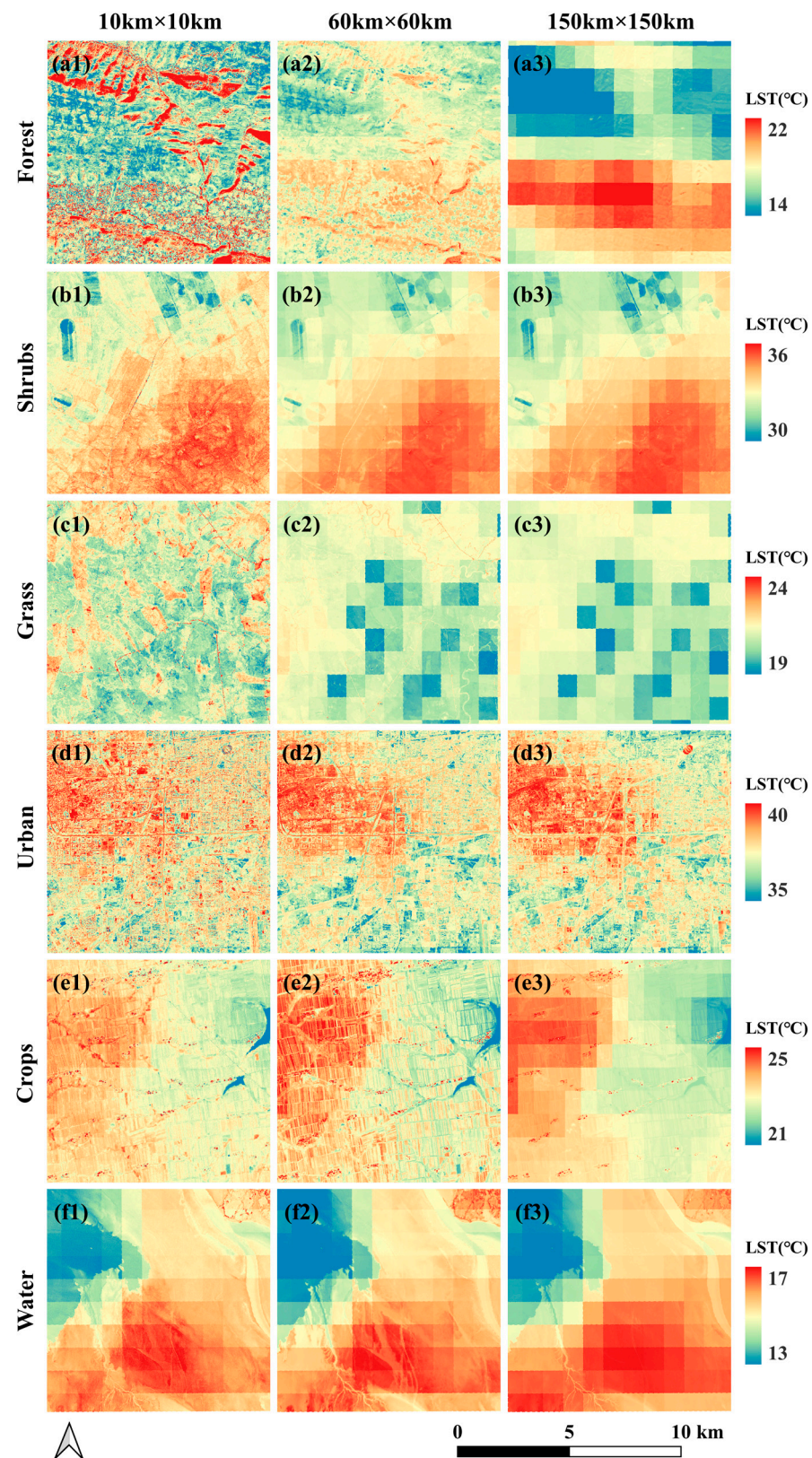


Figure 4. The results of the original DLST method for different study areas at different extents. Each row represents the results for the same land cover type, while each column corresponds to the results for the same spatial extent. Due to the limitation of the minimum extent of $10 \text{ km} \times 10 \text{ km}$, the $60 \text{ km} \times 60 \text{ km}$ and $150 \text{ km} \times 150 \text{ km}$ extents in the figures are both intercepted to show the extent of $10 \text{ km} \times 10 \text{ km}$.

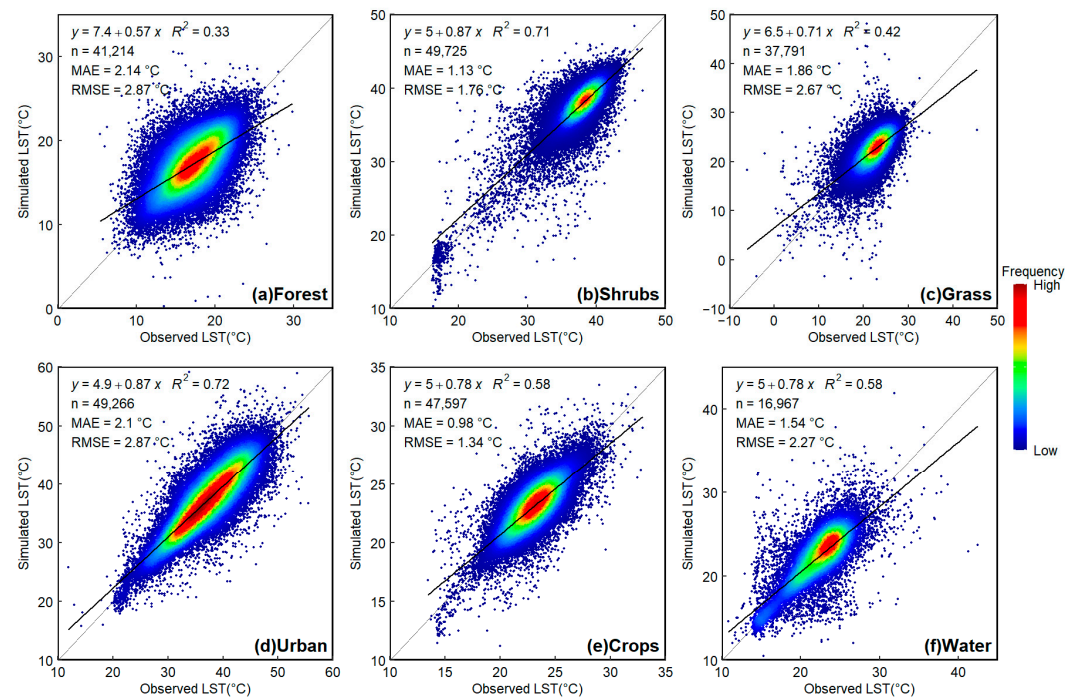


Figure 5. The results of the evaluation in the six study areas. The observed LST is from the calibrated Landsat-8 product. The simulated LST is from the mDTSG model. The light grey line is the 1:1 line. The black line is the linear regression result.

Table 2. Results of DTSG and mDTSG evaluation indices.

Land Cover Type	DTSG vs. Landsat-8			mDTSG vs. Landsat-8			R^2 Improvement (%)
	R^2	MAE	RMSE	R^2	MAE	RMSE	
Forest	0.21	2.14	2.87	0.33	2.14	2.87	57.14
Shrubs	0.58	1.13	1.75	0.71	1.13	1.76	22.41
Grass	0.48	1.85	2.68	0.42	1.86	2.67	−12.50
Urban	0.56	2.11	2.88	0.72	2.10	2.87	28.57
Crops	0.63	0.98	1.35	0.58	0.98	1.34	−7.94
Water	0.27	1.52	2.23	0.58	1.54	2.27	114.81
Average	0.46	1.62	2.29	0.56	1.63	2.30	33.75

Figure 6 shows the results of validation at Danjiangkou station. From the diagonal scatter plot (Figure 6a), it can be observed that the regression line is distributed to the lower right of the 1:1 line, with an R^2 of 0.7. This indicates that there is a tendency for the simulated value of mDTSG to underestimate the observed LST at Danjiangkou station. However, again, the degree of deviation is not high and falls within a reasonable error range. The MAE is 2.03 °C, and the RMSE is 2.63 °C, indicating that mDTSG is highly credible. The distribution trend in the time-series indicates that the two lines are very consistent, and the undulation trend is basically the same (Figure 6b). The mDTSG results were almost consistent with the observed values in the first few months, while the mDTSG results underestimated the LST in later months. This may be related to seasonal variations; however, it does not affect the overall accuracy. The results show that mDTSG can predict the true value effectively at different times and has high potential for use in future research.

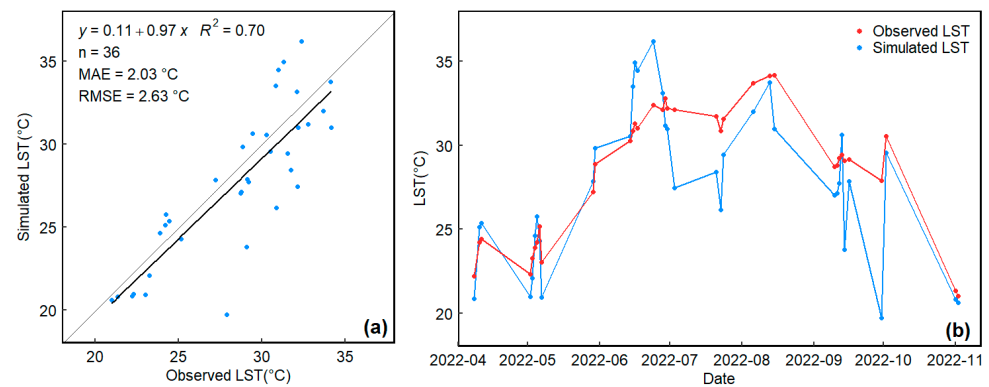


Figure 6. The results of validation at Danjiangkou station, including (a) the diagonal scatter plot and (b) the distribution trend in the time-series. The observed LST is from the calibrated in situ data. The simulated LST is from the mDTSG model.

3.3. Application of Proposed mDTSG Method

Figure 7 shows the local results of mDTSG in the six study areas. The global study extent was $150 \text{ km} \times 150 \text{ km}$ (Figure A3), while a $10 \text{ km} \times 10 \text{ km}$ extent with significant features was selected for detailed observation (Figure 7(a2–f2)). Overall, mDTSG successfully improved the spatial resolution by 100 times, and many features are clearly visible at the 10 m resolution, such as land and water boundaries (Figure 7(f3)), urban geometries (Figure 7(d3)), and agricultural parcel boundaries (Figure 7(e3)).

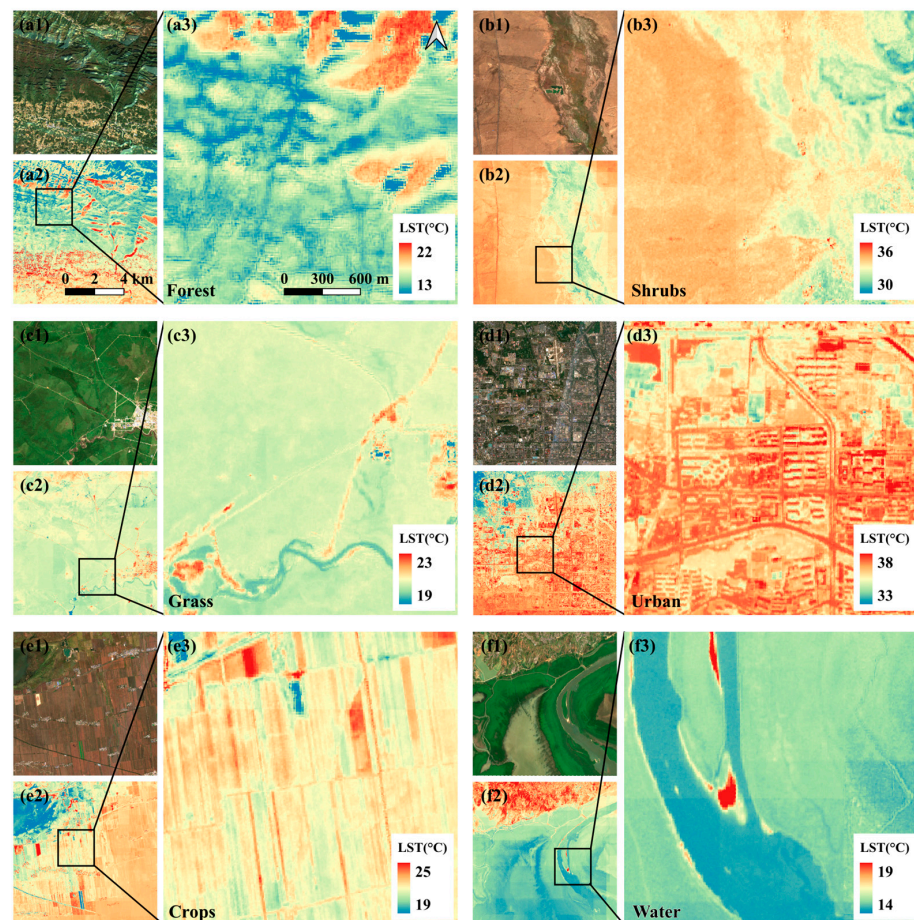


Figure 7. The local results of mDTSG in the six study areas. (a1–f1) Sentinel-2 true-color raster images, (a2–f2) local results of mDTSG in the $10 \text{ km} \times 10 \text{ km}$ extent, and (a3–f3) details within the black square in (a2–f2).

Locally, the LST variations in mDTSG have a one-to-one correspondence with the features. For example, in the forest region (Figure 7(a2)), the temperature of human settlements to the south was significantly higher than that of the forest region in the north. The temperature in the non-shaded region of the forest region was significantly higher than that in the shaded region. In the shrubs region (Figure 7(b2)), the temperature of the river valley on the right was significantly lower than that of the surrounding shrubs, presenting an obvious boundary. In the grass region (Figure 7(c2)), the temperature of the eastern urban region was significantly higher than the surroundings, and the roads are clearly visible. In the urban region (Figure 7(d2)), the geometry and edge contours of the buildings are clearly visible, and vegetation temperatures were significantly lower. In the crop region (Figure 7(e2)), the water temperature in the northwest was significantly lower than that of crops, and the agricultural parcel boundaries are obvious. In the water region (Figure 7(f2)), the temperature was high where the water is shallow and sediment contents are high; in contrast, the temperature was low where the water is deep. Generally speaking, mDTSG can effectively identify the feature information and obtain fine-resolution DLST.

Figure 8 shows the comparison results of observation and simulation for the six study areas at $150 \text{ km} \times 150 \text{ km}$. To compare the details of the features, only the selected $10 \text{ km} \times 10 \text{ km}$ extent is shown in the figure. Compared with DTSG, mDTSG significantly mitigates the scale effect and more accurately identifies and differentiates the fine details of various landscapes. Compared with MOD11A1 images, mDTSG substantially reduces boundary effects between adjacent tiles and sharpens the edges of distinct landscape features. Compared with Landsat-8 images, the features in both images exhibit strong consistency, with mDTSG effectively preserving and restoring the true features information. mDTSG's reduction of scale effect within the range of $150 \text{ km} \times 150 \text{ km}$ is much better than that of $60 \text{ km} \times 60 \text{ km}$ and $10 \text{ km} \times 10 \text{ km}$ (Figure A4). Visually, the most obvious reduction in scale effect was observed in the forest and crop regions (Figure 8(a2,e2)), where mDTSG successfully downscaled the spatial resolution to 10 m. The temperature distinction between the localities is clear, with high- and low-temperature regions being prominent. In contrast, in the urban region (Figure 8(d2)), there was little difference between the surface feature details. The temperature of mDTSG is slightly higher, which may be related to the degree of heterogeneity of the different surface cover types.

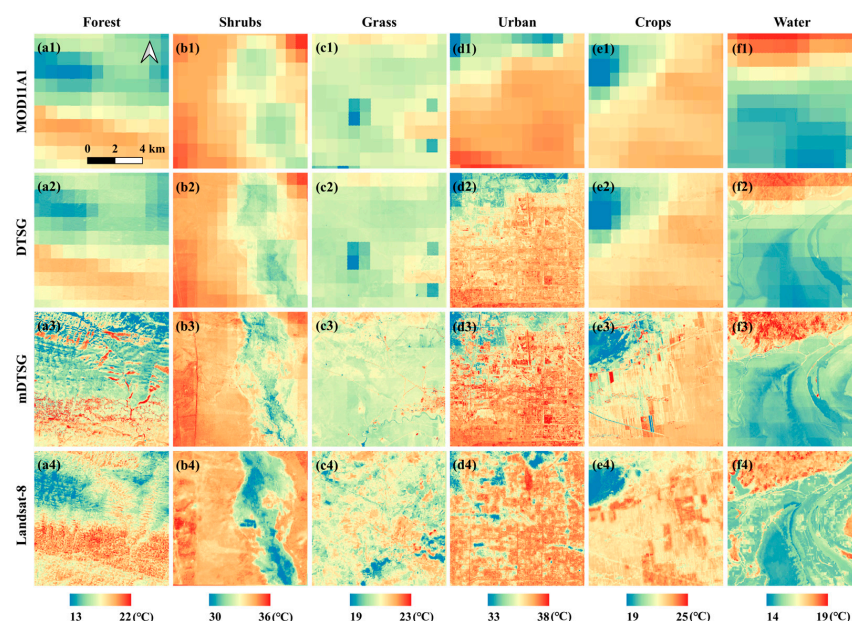


Figure 8. Comparison of observed and simulated images in six different landscapes (in different columns). (a1–f1) MOD11A1 images, (a2–f2) DTSG simulation results, (a3–f3) mDTSG simulated results, and (a4–f4) calibrated Landsat-8 images. Only the $10 \text{ km} \times 10 \text{ km}$ extent with obvious features is selected to show in this figure.

4. Discussion

4.1. Influence of Moving Window Size on Scale Effect

This section provides a detailed discussion on the selection of the moving window. The receptive field range a was varied from 0.05° to 1° with a step size of 0.05° , and the convolution kernel range b was varied from 0.01° to 0.05° with a step size of 0.01° . All combinations were tested according to the fixed step size. The following discussion only presents images with distinct features under different parameters. The water region was selected as an example, and the specific location is shown in Figure A3.

Figure 9 shows the DLST results with b kept constant and varying a . It can be observed that, when b is fixed at 0.01° , the images become more homogeneous as the size of a increases and the range of LST variation decreases. This indicates that the influence of the scale effect increases when the receptive field range is gradually expanded. The reason for this phenomenon is that the increased receptive field range renders the land cover information incorporated in the window increasingly complex. This information does not represent the land surface heterogeneity within the convolution kernel range well, resulting in substantial errors. It is worth noting that, when a was set to 0.05° , the image shows partial missing and obvious errors (red and blue parts on the right side in Figure 9a). Meanwhile, when the receptive field range is reduced to a certain extent, the number of pixels contained within it is not sufficient to support the calculation, resulting in statistical errors. The partial missing image is also due to the fact that the number of pixels within the receptive field range is not sufficient to support the computation; thus, this window is automatically skipped, resulting in no output. After continuous adjustment of the size of a and comparison of the output results for each region, $0.1^\circ \times 0.1^\circ$ was finally chosen as the receptive field range for the moving window.

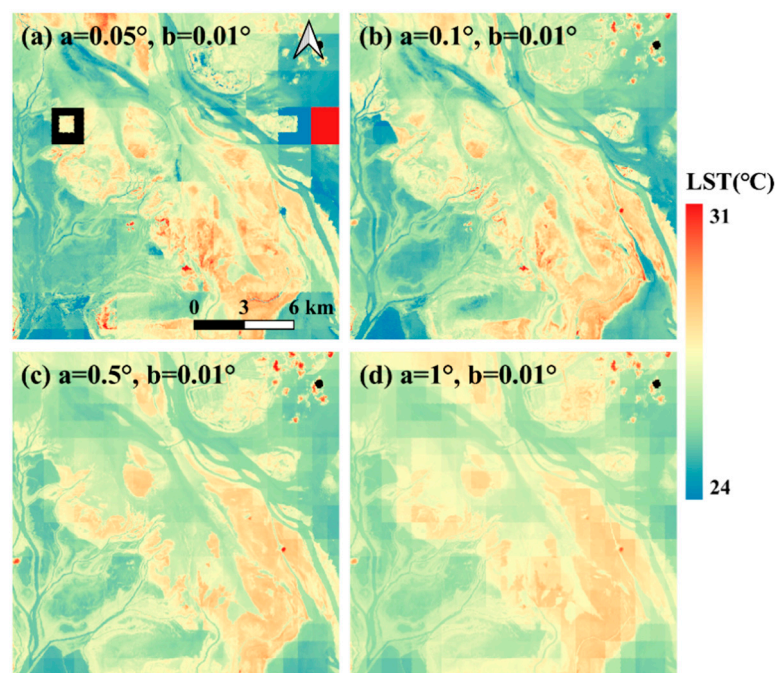


Figure 9. The DLST results when b is kept constant and the size of a is varied. Only the obvious features at $b = 0.01^\circ$ and (a) $a = 0.05^\circ$, (b) $a = 0.1^\circ$, (c) $a = 0.5^\circ$, and (d) $a = 1^\circ$ are shown in the figure for a range of $20 \text{ km} \times 20 \text{ km}$. Black areas in the figure are missing values in the images.

Figure 10 shows the DLST results with a kept constant and varying b . Under the premise that a is set to 0.1° , the image similarly begins to gradually homogenize as b increases (this is particularly evident in the lower left part of Figure 10). The increase in the convolution kernel range makes the data retained in each window less connected to the surrounding data, resulting in errors. In particular, as b increases to the size of a , the

image becomes directly spliced into each window, which causes obvious boundaries. It is worth noting that b should ideally be reduced to the size of a pixel at fine resolutions. However, as b shrinks, the computation time increases exponentially. After a comprehensive evaluation of the computational efficiency and result effects, $0.01^\circ \times 0.01^\circ$ was selected as the convolution kernel range of the moving window.

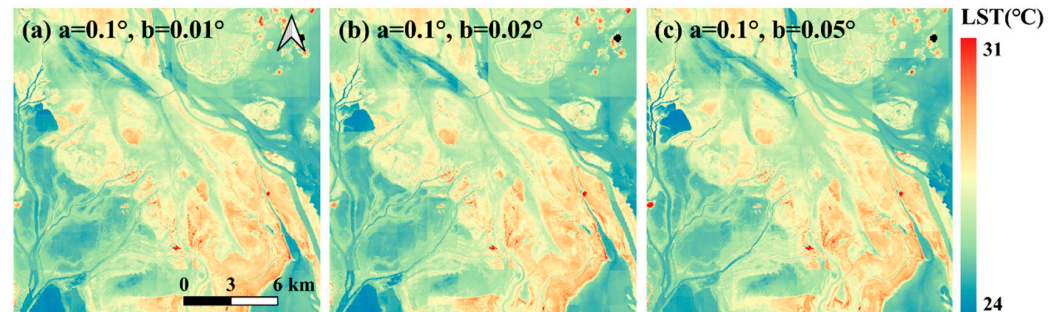


Figure 10. The DLST results when a is kept constant and the size of b is varied. Only the obvious features at $a = 0.1^\circ$ and (a) $b = 0.01^\circ$, (b) $b = 0.02^\circ$, and (c) $b = 0.05^\circ$ are shown in the figure for a range of $20 \text{ km} \times 20 \text{ km}$. Black areas in the figure are missing values in the images.

4.2. Uncertainties in Different Heterogeneous Regions

The results of the evaluation of the 10 m mDTSG product revealed reasonable differences from the Landsat-8 product. Compared to DTSG (using a global window), mDTSG (local window) obtained the most pronounced reduction in spatial scale effects at $150 \text{ km} \times 150 \text{ km}$ for the forest and crop regions, whereas fewer differences in the effect were observed for the urban region (Figure 8). This is due to the influence of heterogeneous differences in different study areas. Forest and crop regions have homogeneous features with small differences in the data of each pixel, which are indistinguishable under the global window, resulting in irrational regression relationships and overfitting. In the local window, as the amount of data contained within each window decreases, the differences between individual pixel data can be effectively captured, resulting in a reduction of the scale effect. In the urban region, the features are complex and variable, and good regression relationships can be obtained with both global and local windows. Considering computational efficiency, the global window is more appropriate, which is consistent with the findings of Li et al. [53]. The global window is superior to the local window for surfaces with a high degree of heterogeneity, while the local window is superior to the global window for surfaces with a low degree of heterogeneity.

The 10 m mDTSG product had an average MAE of 1.63°C and an average RMSE of 2.3°C when compared to the Landsat-8 product, which is within a reasonable margin of error. Wang et al. [54] also reached a similar conclusion when using non-linear geographically weighted regression to obtain a MODIS-based 100 m LST with an average MAE of 1.5°C compared to Landsat-8. As such, the difference between the two is subtle. Considering that the proposed algorithm uses RLS for regression analysis, the weight assigned to the extreme points is reduced, with a general trend closer to high-frequency regions. The distribution of the regression line (Figure 5) is also reasonable. The MAE and RMSE results of mDTSG and DTSG are considered to be seriously affected by the volatility of the data. In a large extent of $150 \text{ km} \times 150 \text{ km}$, the sampled data is huge, and the distribution is complex, resulting in similar results. However, the R^2 of mDTSG is significantly better than that of DTSG overall, which shows that the new method has superior ability to explain the data and can better capture the complex temperature changes.

Danjiangkou station data were selected for ground validation. The validation results (i.e., MAE value of 2.03°C and RMSE value of 2.63°C) were lower than those obtained by Mhawej and Abunnasr [45]. However, it is worth noting that the validation data here are only a time-series and, as such, do not provide good evidence regarding the spatial distribution. The lack of comprehensive and freely available airborne surveys limits the

availability of validation data, which is undoubtedly a great challenge for this study. However, Agathangelidis and Cartalis [55] achieved an average *RMSE* of 1.53 °C for the generated 100 m LST compared to in situ measurements. Bonafoni et al. [56] successfully improved the *RMSE* to 3 °C for the obtained 30 m LST compared to airborne sensor data. In reference to previous studies, the results of this study can be considered reasonably reliable. Although LST data at the same time as the daily transit time of the Terra satellite equipped with MODIS were selected for the study, seasonal variations in the time scale are still a factor that cannot be ignored.

4.3. Application Prospects of Proposed New Method

Although the spatial scale effect of the DLST results in this study was significantly reduced at fine resolutions and the obtained evaluation and validation results were good, there are still some limitations. Considering the difference in acquisition time between different sensors, as well as in situ data, the dT was introduced for correction. However, the differences between sensors are often multi-faceted; for example, differences in the instantaneous field of view, orbiting geometry, swath width, and spectral response functions can complicate the comparison of thermal images between different sensors. This is also an area where future research should be focused. To solve the current data contamination problem caused by cloud and terrain shadows, the data source can introduce thermal radiation products from different satellite sensors, such as ASTER, Landsat-5, Landsat-7, and Landsat-9, to further improve the temporal resolution. Moreover, due to the lack of data for ground validation, the initiative of sharing existing and new ground-based TIR images from different regions to create a comprehensive and diverse ground reference network is crucial and recommended [52]. In addition, in order to improve the computational efficiency of mDTSG, GEE can be used in conjunction with more efficient local models, which will further advance its applicability.

The evaluation and validation of mDTSG proved the effectiveness of the developed improvements. Such fine-resolution LSTs further expand the application of remote sensing thermal radiation products in different fields. For example, the LST of features such as buildings and houses, which were originally undetectable in the urban environment, could be well identified through the use of mDTSG. In the agricultural field, mDTSG is able to recognize heterogeneity within agricultural lands, providing a more accurate assessment of daily water requirements and vegetation health. This increased spatial and temporal resolution detail is expected to allow environmental management plans to evolve to an unprecedented level of detail, which is desperately needed in the current era of climate change.

5. Conclusions

This study evaluated the scale effect of DLST results at fine resolutions (10 m) based on a downscaling method named DTSG. Six regions with different land cover types were selected as the case study areas. The results show that the spatial scale effect becomes increasingly obvious as the extent increases and is closely related to the heterogeneity degree of the surface features, with the lowest impacts in urban regions and the greatest impacts in water regions. To effectively reduce the influence of the scale effect, a modified DTSG method was proposed in this study, which successfully achieved higher-accuracy DLST results through the introduction of a convolution-based moving window. The results show that the improvements provided by the method are significant, especially when considering large extents and surfaces with a low degree of heterogeneity, with an average R^2 improvement of 33.75%. From the images, the most significant improvement effect was observed for forest and crop regions, while little differences were found for the urban region. Considering both the computational efficiency and the accuracy of the model's results after introducing the moving window, the global window performs better than the local window for surfaces with high heterogeneity, while the local window performs better than the global window for surfaces with low heterogeneity.

The evaluation and validation results revealed a slight difference between the 10 m mDTSG product and the Landsat-8 product: the average *MAE* was 1.63 °C, and the average *RMSE* was 2.3 °C. Comparisons with in situ data showed very promising results, with an *MAE* of 2.03 °C and an *RMSE* of 2.63 °C. Thus, mDTSG can be implemented for different land cover types and seasons. The results indicate that the mDTSG model has high potential for application in future research, and it is expected to have high significance for urban thermal environment studies, agricultural evapotranspiration mapping, and extreme weather forecasting.

Author Contributions: Conceptualization, Z.G. and L.C. (Lei Cheng); methodology, Z.G. and L.C. (Lei Cheng); software, Z.G., L.C. (Liwei Chang) and S.L.; data curation, Z.G. and Y.L.; writing—original draft preparation, Z.G. and L.C. (Lei Cheng); writing—review and editing, Z.G., L.C. (Lei Cheng), L.C. (Liwei Chang) and S.L.; supervision, L.C. (Lei Cheng) and L.C. (Liwei Chang); funding acquisition, L.C. (Lei Cheng). All authors have read and agreed to the published version of the manuscript.

Funding: This research was funded by the National Natural Science Foundation of China (U2340207, 52350710209, and 52394233) and the Natural Science Foundation of Hubei Province (2022CFA094).

Data Availability Statement: Publicly available datasets were used in this study. Sentinel-2 MSI: MultiSpectral Instrument, Level-2A is available at https://developers.google.com/earth-engine/datasets/catalog/COPERNICUS_S2_SR (accessed on 31 December 2023). MOD09A1.006 Terra Surface Reflectance 8-Day Global 500 m is available at https://developers.google.com/earth-engine/datasets/catalog/MODIS_006_MOD09A1 (accessed on 31 December 2023). MOD11A1.006 Terra Land Surface Temperature and Emissivity Daily Global 1 km is available at https://developers.google.com/earth-engine/datasets/catalog/MODIS_006_MOD11A1 (accessed on 31 December 2023). USGS Landsat 8 Level 2, Collection 2, Tier 1 is available at https://developers.google.com/earth-engine/datasets/catalog/LANDSAT_LC08_C02_T1_L2 (accessed on 31 December 2023).

Acknowledgments: We would like to thank the fundings and all data providers mentioned above. We sincerely thank the anonymous reviewers and editors of the journal for providing helpful comments to improve the manuscript.

Conflicts of Interest: The authors declare no conflicts of interest.

Appendix A

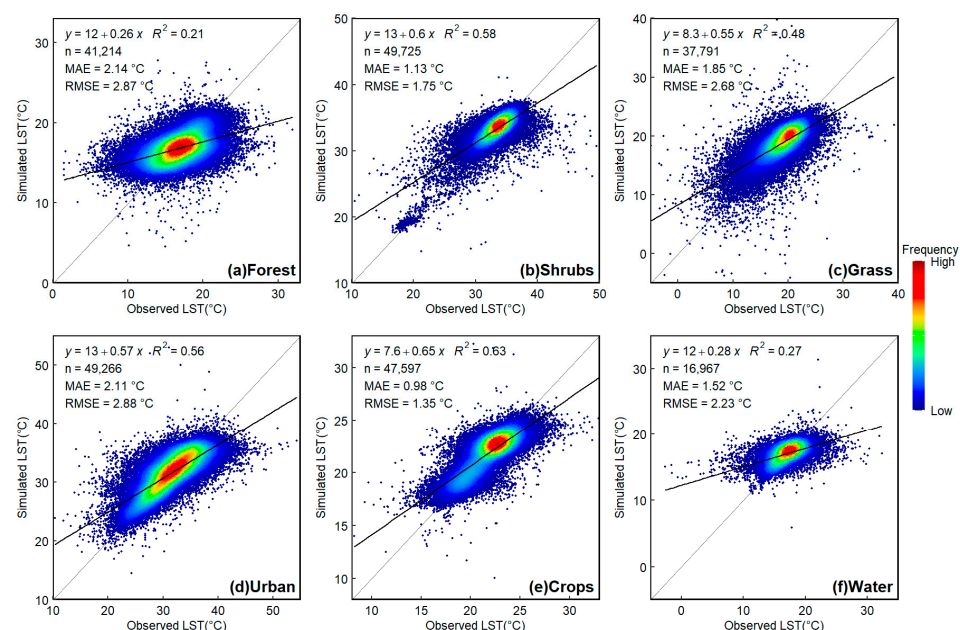


Figure A1. The results of the evaluation in the six study areas. The observed LST is from the calibrated Landsat-8 product. The simulated LST is from the DTSG model. The light grey line is the 1:1 line. The black line is the linear regression result.

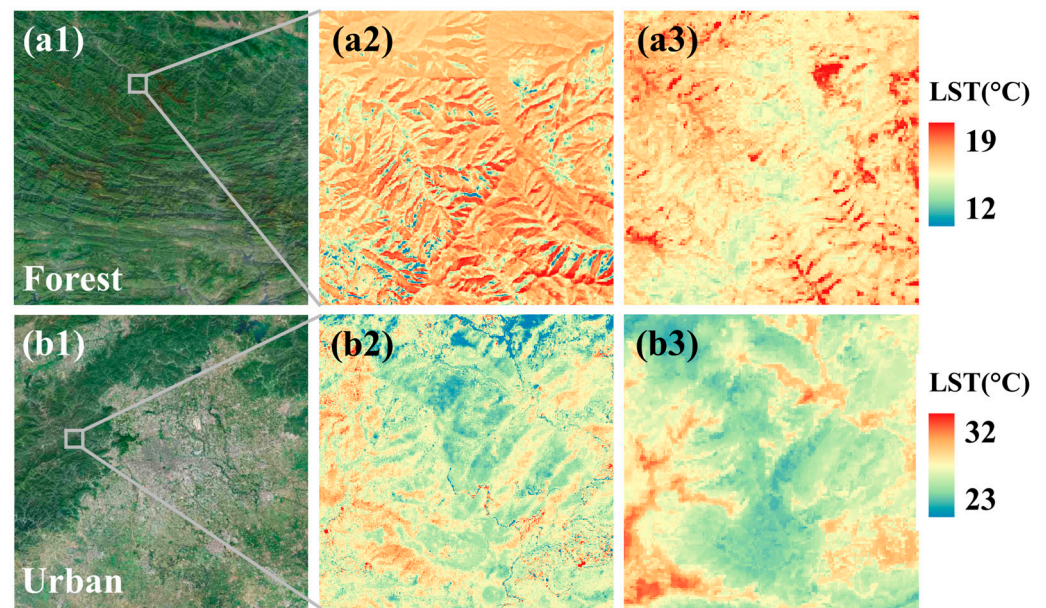


Figure A2. The shadow distribution location of forest and urban regions. (a1,b1) Sentinel-2 true-color raster images, (a2,b2) local results of mDTSG, and (a3,b3) local Landsat-8 image within the gray square in (*1).

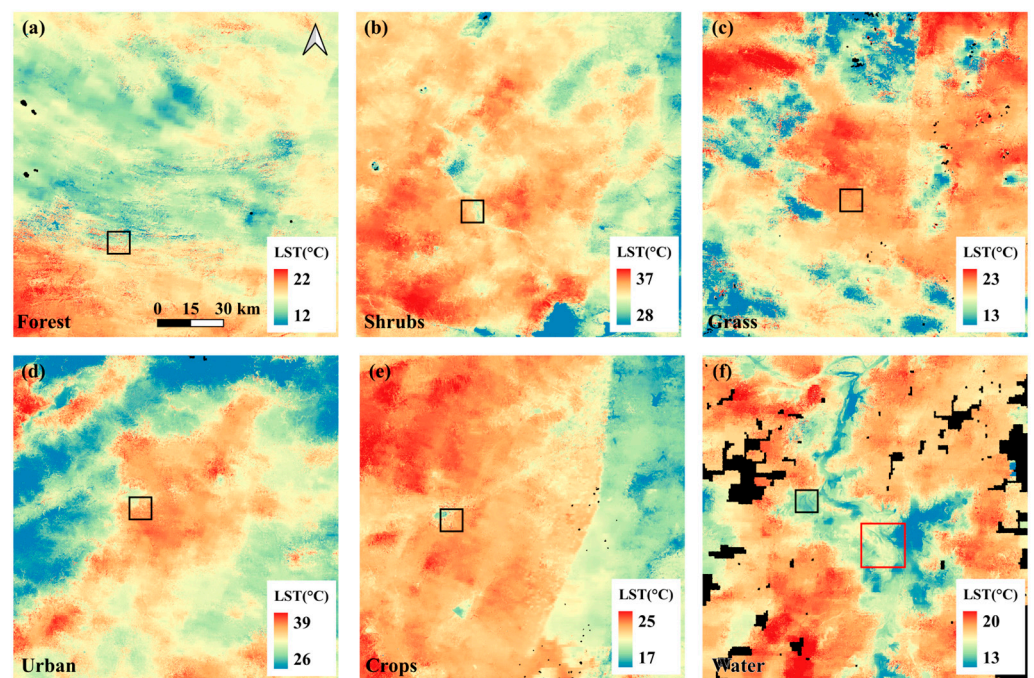


Figure A3. The global results of mDTSG in the six study areas. A study extent of $150 \text{ km} \times 150 \text{ km}$ was selected in (a) forest, (b) shrubs, (c) grass, (d) urban, (e) crops, and (f) water regions. The black square extent is selected and shown in Figure 7. The red square extent is selected and shown in Figures 9 and 10. Black areas in the figure are missing values in the images.

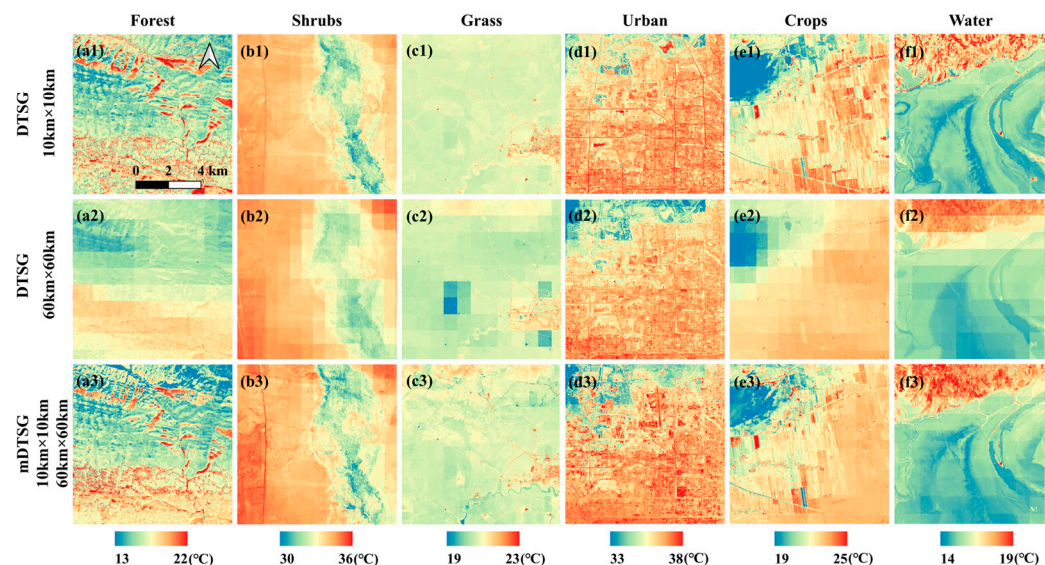


Figure A4. Comparison of DTSG and mDTSG methods in six different landscapes (in different columns). The first and second rows (a1–f1,a2–f2) show the performance of DTSG at 10 km × 10 km and 60 km × 60 km spatial extents. The third row (a3–f3) shows the performance of mDTSG.

References

- Carlson, T. An overview of the “triangle method” for estimating surface evapotranspiration and soil moisture from satellite imagery. *Sensors* **2007**, *7*, 1612–1629. [\[CrossRef\]](#)
- Anderson, M.C.; Allen, R.G.; Morse, A.; Kustas, W.P. Use of Landsat thermal imagery in monitoring evapotranspiration and managing water resources. *Remote Sens. Environ.* **2012**, *122*, 50–65. [\[CrossRef\]](#)
- Anderson, M.C.; Kustas, W.P.; Norman, J.M.; Hain, C.R.; Mecikalski, J.R.; Schultz, L.; Gonzalez-Dugo, M.P.; Cammalleri, C.; D’Urso, G.; Pimstein, A.; et al. Mapping daily evapotranspiration at field to continental scales using geostationary and polar orbiting satellite imagery. *Hydrol. Earth Syst. Sci.* **2011**, *15*, 223–239. [\[CrossRef\]](#)
- Jin, M.L.; Dickinson, R.E.; Zhang, D.L. The footprint of urban areas on global climate as characterized by MODIS. *J. Clim.* **2005**, *18*, 1551–1565. [\[CrossRef\]](#)
- Zhan, W.; Chen, Y.; Zhou, J.; Wang, J.; Liu, W.; Voogt, J.; Zhu, X.; Quan, J.; Li, J. Disaggregation of remotely sensed land surface temperature: Literature survey, taxonomy, issues, and caveats. *Remote Sens. Environ.* **2013**, *131*, 119–139. [\[CrossRef\]](#)
- Tomlinson, C.J.; Chapman, L.; Thornes, J.E.; Baker, C. Remote sensing land surface temperature for meteorology and climatology: A review. *Meteorol. Appl.* **2011**, *18*, 296–306. [\[CrossRef\]](#)
- Li, Z.; Tang, B.; Wu, H.; Ren, H.; Yan, G.; Wan, Z.; Trigo, I.F.; Sobrino, J.A. Satellite-derived land surface temperature: Current status and perspectives. *Remote Sens. Environ.* **2013**, *131*, 14–37. [\[CrossRef\]](#)
- Zhou, D.; Xiao, J.; Bonafoni, S.; Berger, C.; Deilami, K.; Zhou, Y.; Frolking, S.; Yao, R.; Qiao, Z.; Sobrino, J.A. Satellite Remote Sensing of Surface Urban Heat Islands: Progress, Challenges, and Perspectives. *Remote Sens.* **2019**, *11*, 48. [\[CrossRef\]](#)
- Peng, J.; Jia, J.; Liu, Y.; Li, H.; Wu, J. Seasonal contrast of the dominant factors for spatial distribution of land surface temperature in urban areas. *Remote Sens. Environ.* **2018**, *215*, 255–267. [\[CrossRef\]](#)
- Xu, Y.; Liu, Y. Monitoring the Near-surface Urban Heat Island in Beijing, China by Satellite Remote Sensing. *Geogr. Res.* **2015**, *53*, 16–25. [\[CrossRef\]](#)
- Shivers, S.W.; Roberts, D.A.; McFadden, J.P. Using paired thermal and hyperspectral aerial imagery to quantify land surface temperature variability and assess crop stress within California orchards. *Remote Sens. Environ.* **2019**, *222*, 215–231. [\[CrossRef\]](#)
- Patel, N.R.; Parida, B.R.; Venus, V.; Saha, S.K.; Dadhwal, V.K. Analysis of agricultural drought using vegetation temperature condition index (VTCI) from Terra/MODIS satellite data. *Environ. Monit. Assess.* **2012**, *184*, 7153–7163. [\[CrossRef\]](#)
- Ahmad, U.; Alvino, A.; Marino, S. A Review of Crop Water Stress Assessment Using Remote Sensing. *Remote Sens.* **2021**, *13*, 4155. [\[CrossRef\]](#)
- Chuvieco, E.; Mouillot, F.; van der Werf, G.R.; Miguel, J.S.; Tanase, M.; Koutsias, N.; Garcia, M.; Yebra, M.; Padilla, M.; Gitas, I.; et al. Historical background and current developments for mapping burned area from satellite Earth observation. *Remote Sens. Environ.* **2019**, *225*, 45–64. [\[CrossRef\]](#)
- Eckmann, T.C.; Still, C.J.; Roberts, D.A.; Michaelsen, J.C. Variations in Subpixel Fire Properties with Season and Land Cover in Southern Africa. *Earth Interact.* **2010**, *14*, 1–29. [\[CrossRef\]](#)
- Eckmann, T.C.; Roberts, D.A.; Still, C.J. Using multiple endmember spectral mixture analysis to retrieve subpixel fire properties from MODIS. *Remote Sens. Environ.* **2008**, *112*, 3773–3783. [\[CrossRef\]](#)

17. Xing, Z.; Fan, L.; Zhao, L.; De Lannoy, G.; Frappart, F.; Peng, J.; Li, X.; Zeng, J.; Al-Yaari, A.; Yang, K.; et al. A first assessment of satellite and reanalysis estimates of surface and root-zone soil moisture over the permafrost region of Qinghai-Tibet Plateau. *Remote Sens. Environ.* **2021**, *265*, 112666. [\[CrossRef\]](#)
18. Ma, H.; Zeng, J.; Chen, N.; Zhang, X.; Cosh, M.H.; Wang, W. Satellite surface soil moisture from SMAP, SMOS, AMSR2 and ESA CCI: A comprehensive assessment using global ground-based observations. *Remote Sens. Environ.* **2019**, *231*. [\[CrossRef\]](#)
19. Bai, L.; Long, D.; Yan, L. Estimation of Surface Soil Moisture with Downscaled Land Surface Temperatures Using a Data Fusion Approach for Heterogeneous Agricultural Land. *Water Resour. Res.* **2019**, *55*, 1105–1128. [\[CrossRef\]](#)
20. Pu, R.; Bonafoni, S. Thermal infrared remote sensing data downscaling investigations: An overview on current status and perspectives. *Remote Sens. Appl.-Soc. Environ.* **2023**, *29*, 111215. [\[CrossRef\]](#)
21. Zhou, Y.; Weng, Q.; Gurney, K.R.; Shuai, Y.; Hu, X. Estimation of the relationship between remotely sensed anthropogenic heat discharge and building energy use. *ISPRS-J. Photogramm. Remote Sens.* **2012**, *67*, 65–72. [\[CrossRef\]](#)
22. Ren, P.; Meng, Q.; Zhang, Y.; Zhao, L.; Yuan, X.; Feng, X. An Unmanned Airship Thermal Infrared Remote Sensing System for Low-Altitude and High Spatial Resolution Monitoring of Urban Thermal Environments: Integration and an Experiment. *Remote Sens.* **2015**, *7*, 14259–14275. [\[CrossRef\]](#)
23. Herrero-Huerta, M.; Laguela, S.; Alfieri, S.M.; Menenti, M. Generating high-temporal and spatial resolution TIR image data. *Int. J. Appl. Earth Obs. Geoinf.* **2019**, *78*, 149–162. [\[CrossRef\]](#)
24. Guo, L.J.; Moore, J.M. Pixel block intensity modulation: Adding spatial detail to TM band 6 thermal imagery. *Int. J. Remote Sens.* **1998**, *19*, 2477–2491. [\[CrossRef\]](#)
25. Yang, Y.; Cao, C.; Pan, X.; Li, X.; Zhu, X. Downscaling Land Surface Temperature in an Arid Area by Using Multiple Remote Sensing Indices with Random Forest Regression. *Remote Sens.* **2017**, *9*, 789. [\[CrossRef\]](#)
26. Weng, Q.; Fu, P.; Gao, F. Generating daily land surface temperature at Landsat resolution by fusing Landsat and MODIS data. *Remote Sens. Environ.* **2014**, *145*, 55–67. [\[CrossRef\]](#)
27. Wu, P.; Shen, H.; Zhang, L.; Goettsche, F. Integrated fusion of multi-scale polar-orbiting and geostationary satellite observations for the mapping of high spatial and temporal resolution land surface temperature. *Remote Sens. Environ.* **2015**, *156*, 169–181. [\[CrossRef\]](#)
28. Jeganathan, C.; Hamm, N.A.S.; Mukherjee, S.; Atkinson, P.M.; Raju, P.L.N.; Dadhwal, V.K. Evaluating a thermal image sharpening model over a mixed agricultural landscape in India. *Int. J. Appl. Earth Obs. Geoinf.* **2011**, *13*, 178–191. [\[CrossRef\]](#)
29. Pu, R.; Bonafoni, S. Reducing Scaling Effect on Downscaled Land Surface Temperature Maps in Heterogenous Urban Environments. *Remote Sens.* **2021**, *13*, 5044. [\[CrossRef\]](#)
30. Pu, R. Assessing scaling effect in downscaling land surface temperature in a heterogenous urban environment. *Int. J. Appl. Earth Obs. Geoinf.* **2021**, *96*, 102256. [\[CrossRef\]](#)
31. Wang, Q.; Shi, W.; Atkinson, P.M. Area-to-point regression kriging for pan-sharpening. *ISPRS-J. Photogramm. Remote Sens.* **2016**, *114*, 151–165. [\[CrossRef\]](#)
32. Jin, Y.; Ge, Y.; Wang, J.; Heuvelink, G.B.M.; Wang, L. Geographically Weighted Area-to-Point Regression Kriging for Spatial Downscaling in Remote Sensing. *Remote Sens.* **2018**, *10*, 579. [\[CrossRef\]](#)
33. Liu, K.; Su, H.; Tian, J.; Li, X.; Wang, W.; Yang, L.; Liang, H. Assessing a scheme of spatial-temporal thermal remote-sensing sharpening for estimating regional evapotranspiration. *Int. J. Remote Sens.* **2018**, *39*, 3111–3137. [\[CrossRef\]](#)
34. Kustas, W.P.; Norman, J.M.; Anderson, M.C.; French, A.N. Estimating subpixel surface temperatures and energy fluxes from the vegetation index-radiometric temperature relationship. *Remote Sens. Environ.* **2003**, *85*, 429–440. [\[CrossRef\]](#)
35. Wu, H.; Li, W. Downscaling Land Surface Temperatures Using a Random Forest Regression Model with Multitype Predictor Variables. *IEEE Access.* **2019**, *7*, 21904–21916. [\[CrossRef\]](#)
36. Chen, X.; Yamaguchi, Y.; Chen, J.; Shi, Y. Scale Effect of Vegetation-Index-Based Spatial Sharpening for Thermal Imagery: A Simulation Study by ASTER Data. *IEEE Geosci. Remote Sens. Lett.* **2012**, *9*, 549–553. [\[CrossRef\]](#)
37. Zhou, J.; Liu, S.; Li, M.; Zhan, W.; Xu, Z.; Xu, T. Quantification of the Scale Effect in Downscaling Remotely Sensed Land Surface Temperature. *Remote Sens.* **2016**, *8*, 975. [\[CrossRef\]](#)
38. Liu, H.; Weng, Q. Scaling Effect of Fused ASTER-MODIS Land Surface Temperature in an Urban Environment. *Sensors* **2018**, *18*, 4058. [\[CrossRef\]](#)
39. Ghosh, A.; Joshi, P.K. Hyperspectral imagery for disaggregation of land surface temperature with selected regression algorithms over different land use land cover scenes. *ISPRS-J. Photogramm. Remote Sens.* **2014**, *96*, 76–93. [\[CrossRef\]](#)
40. Marceau, D.J.; Hay, G.J. Remote Sensing Contributions to the Scale Issue. *Can. J. Remote Sens.* **1999**, *25*, 357–366. [\[CrossRef\]](#)
41. Bindhu, V.M.; Narasimhan, B.; Sudheer, K.P. Development and verification of a non-linear disaggregation method (NL-DisTrad) to downscale MODIS land surface temperature to the spatial scale of Landsat thermal data to estimate evapotranspiration. *Remote Sens. Environ.* **2013**, *135*, 118–129. [\[CrossRef\]](#)
42. Garrigues, S.; Allard, D.; Baret, F.; Weiss, M. Quantifying spatial heterogeneity at the landscape scale using variogram models. *Remote Sens. Environ.* **2006**, *103*, 81–96. [\[CrossRef\]](#)
43. Zaksek, K.; Ostir, K. Downscaling land surface temperature for urban heat island diurnal cycle analysis. *Remote Sens. Environ.* **2012**, *117*, 114–124. [\[CrossRef\]](#)

44. Gao, L.; Zhan, W.; Huang, F.; Quan, J.; Lu, X.; Wang, F.; Ju, W.; Zhou, J. Localization or Globalization? Determination of the Optimal Regression Window for Disaggregation of Land Surface Temperature. *IEEE Trans. Geosci. Remote Sens.* **2017**, *55*, 477–490. [CrossRef]
45. Mhawej, M.; Abunnastr, Y. Daily Ten-ST-GEE: An open access and fully automated 10-m LST downscaling system. *Comput. Geosci.* **2022**, *168*, 105220. [CrossRef]
46. Claverie, M.; Ju, J.; Masek, J.G.; Dungan, J.L.; Vermote, E.F.; Roger, J.; Skakun, S.V.; Justice, C. The Harmonized Landsat and Sentinel-2 surface reflectance data set. *Remote Sens. Environ.* **2018**, *219*, 145–161. [CrossRef]
47. Zhang, H.K.; Roy, D.P.; Yan, L.; Li, Z.; Huang, H.; Vermote, E.; Skakun, S.; Roger, J. Characterization of Sentinel-2A and Landsat-8 top of atmosphere, surface, and nadir BRDF adjusted reflectance and NDVI differences. *Remote Sens. Environ.* **2018**, *215*, 482–494. [CrossRef]
48. Abunnastr, Y.; Mhawej, M. Towards a combined Landsat-8 and Sentinel-2 for 10-m land surface temperature products: The Google Earth Engine monthly Ten-ST-GEE system. *Environ. Modell. Softw.* **2022**, *155*, 105456. [CrossRef]
49. Vermote, E. *MODIS/Terra Surface Reflectance 8-Day L3 Global 500m SIN Grid V061 [Data Set]*; NASA EOSDIS Land Processes Distributed Active Archive Center: Sioux Falls, SD, USA, 2021.
50. Wan, Z.; Hook, S.; Hulley, G. *MODIS/Terra Land Surface Temperature/Emissivity Daily L3 Global 1km SIN Grid V061 [Data Set]*; NASA EOSDIS Land Processes Distributed Active Archive Center: Sioux Falls, SD, USA, 2021.
51. Sergii, S.; Eric, F.V.; Jean, C.R.; Christopher, O.J.; Jeffrey, G.M. Validation of the LaSRC Cloud Detection Algorithm for Landsat 8 Images. *IEEE J. Sel. Top. Appl. Earth Observ. Remote Sens.* **2019**, *12*, 2439–2446.
52. Guillevic, P.; Göttsche, F.; Nickeson, J.; Hulley, G.; Ghent, D.; Yu, Y.; Trigo, I.; Hook, S.; Sobrino, J.A.; Remedios, J.; et al. Land Surface Temperature Product Validation Best Practice Protocol. Version 1.1. In *Good Practices for Satellite-Derived Land Product Validation*; Guillevic, P., Göttsche, F., Nickeson, J., Román, M., Eds.; Land Product Validation Subgroup (WGCV/CEOS); 2018; p. 58. Available online: https://lpvs.gsfc.nasa.gov/PDF/CEOS_LST_PROTOCOL_Feb2018_v1.1.0_light.pdf (accessed on 16 October 2024).
53. Li, N.; Wu, H.; Ouyang, X. Localized Downscaling of Urban Land Surface Temperature-A Case Study in Beijing, China. *Remote Sens.* **2022**, *14*, 2390. [CrossRef]
54. Wang, S.; Luo, Y.; Li, X.; Yang, K.; Liu, Q.; Luo, X.; Li, X. Downscaling Land Surface Temperature Based on Non-Linear Geographically Weighted Regressive Model Over Urban Areas. *Remote Sens.* **2021**, *13*, 1580. [CrossRef]
55. Agathangelidis, I.; Cartalis, C. Improving the disaggregation of MODIS land surface temperatures in an urban environment: A statistical downscaling approach using high-resolution emissivity. *Int. J. Remote Sens.* **2019**, *40*, 5261–5286. [CrossRef]
56. Bonafoni, S.; Anniballe, R.; Gioli, B.; Toscano, P. Downscaling Landsat Land Surface Temperature over the urban area of Florence. *Eur. J. Remote Sens.* **2016**, *49*, 553–569. [CrossRef]

Disclaimer/Publisher’s Note: The statements, opinions and data contained in all publications are solely those of the individual author(s) and contributor(s) and not of MDPI and/or the editor(s). MDPI and/or the editor(s) disclaim responsibility for any injury to people or property resulting from any ideas, methods, instructions or products referred to in the content.